Research Article

Nano Research
2023, 16(4): 4970–4979

ISSN 1998-0124 CN 11-5974/O4
https://doi.org/10.1007/s12274-022-5180-y

Piezoelectric soft robot driven by mechanical energy

Jiangfeng Lu[1,§], Zicong Miao[2,§], Zihan Wang[1,§], Ying Liu[1], Dekuan Zhu[2], Jihong Yin[1], Fei Tang[3], Xiaohao Wang[1,2] (✉), Wenbo Ding[1] (✉), and Min Zhang[2] (✉)

[1] *Tsinghua-Berkeley Shenzhen Institute, Tsinghua University, Shenzhen 518055, China*
[2] *Shenzhen International Graduate School, Tsinghua University, Shenzhen 518055, China*
[3] *State Key Laboratory of Precision Measurement Technology and Instruments, Department of Precision Instruments, Tsinghua University, Beijing100084, China*
[§] *Jiangfeng Lu, Zicong Miao, and Zihan Wang contributed equally to this work.*

Received: 7 September 2022 / **Revised:** 1 October 2022 / **Accepted:** 10 October 2022

ABSTRACT

Power sources and energy-harvesting schemes are still grand challenges for soft robots. Notably, compared with other power sources, triboelectric nanogenerators (TENGs) have shown great potential because of their low manufacturing and fabrication costs, outstanding resilience, remarkable stability, and environmental friendliness. Herein, a triboelectric effect-driven piezoelectric soft robot (TEPSR) system is proposed, which integrates a rotary freestanding triboelectric nanogenerator (RF-TENG) to drive a soft robot comprising a piezoelectric unimorph and electrostatic footpads. Based on the natural triboelectrification, through converting mechanical energy into electricity, TENG provides a unique approach for actuation and manipulation of the soft robot. The perfect combination provides the most straightforward way for creating a self-powered system. Experimentally, under the power of RF-TENG, the soft robot reaches a maximum moving speed of 10 cm per second and a turning rate of 89.7° per second, respectively. The actuation and manipulation demonstration are intuitively accomplished by maneuvering the robot around a maze with a 71 cm track within 28 s. For autonomous feedback controls, one practical application is carrying two infrared sensors on board to realize obstacle avoidance in an unstructured environment. Moreover, a micro-camera was equipped with the soft robot to provide real-time "first-person" video streaming, enhancing its detection capability.

KEYWORDS

triboelectric nanogenerator, piezoelectric soft robot, rapid actuation, agile trajectory manipulation, energy efficiency

1 Introduction

Soft robots have inspired extensive enthusiasm in academic and industry owing to their unique advantages, such as strong adaptability, large deformation, and good flexibility, compared with their rigid-bodied counterparts [1]. Constructed from compliant, deformable, and active materials, a variety of exciting applications have been accomplished by soft robots such as diverse and robust grasping [2], selective trapping, actively perceiving [3], and transportation [4]. In respect to soft actuators and stimuli-responsive materials, research into that is flourishing with dielectric elastomer actuators (DEAs) [5, 6], piezoelectric-based actuators [7, 8], shape memory alloys (SMAs) [9], shape memory polymers (SMPs) [10, 11], liquid crystal elastomers (LCEs) [12, 13], synthetic hydrogels [14, 15], composite materials [16, 17], and more. These materials can be stimulated by either electrically, magnetically, pneumatically, hydraulically, thermally [18], or even driven by irradiation (near infrared (NIR)) light and magnetic field dual mode [16]. Compared with other stimuli-responsive ones, electrically responsive soft actuators can be directly and precisely controlled and adjusted more easily, due to the easy modulation of magnitude, phase, and frequency of electronic signals [19]. But existing electrical signals are usually generated by relatively heavy and bulky devices, such as signal generators and amplifiers, impeding the application of the robot. Currently available commercial technologies, such as lithium-ion and lead-acid batteries, have limited capacity and usually require complex control circuits and high-voltage converters in practical robot applications [8, 20], adding extra weight/volume and complexity of the system. For long-lasting operation of mobile robots, power and energy sources, including new power sources, battery technologies, and energy-harvesting schemes, still represent one of the most challenging areas [21, 22].

It is noteworthy that triboelectric nanogenerators (TENGs), a technology converting environmental tiny mechanical energy into electricity with relatively acceptable outpower, have attracted intensive interest since it was proposed by Wang et al. in 2012 [23]. Attributed to the device's simplicity, wide availability, and ease of fabrication, TENG has been proven to be one of the most effective ways for harvesting mechanical energies. In recent years, series efforts have been made in developing TENGs to harvest mechanical energy from human motion [24], wind energy [25], water wave energy [26], mechanical displacement pulse [27], etc. However, with a rather high internal resistance, the output voltage

Address correspondence to Xiaohao Wang, wang.xiaohao@sz.tsinghua.edu.cn; Wenbo Ding, ding.wenbo@sz.tsinghua.edu.cn; Min Zhang, zhang.min@sz.tsinghua.edu.cn

from TENG decreases dramatically with the decrease of the load resistances [28], making it incompatible with traditional data acquisition circuits. Moreover, TENG's high voltage (a few thousand volts) and low current output (at the scale of microampere) make it unseemly to directly drive conventional electronic equipment with continuous and constant input [29]. Notably, smart materials with electrically responsive characteristics, such as dielectric elastomers [30, 31], piezoelectric materials [32], and ferroelectric materials [33, 34], usually have rather high internal resistance to maintain the tribo-induced charge [28]. As a result, these materials show great potential in combination with TENGs.

Bu et al. proposed a triboelectric effect-driven liquid metal actuator, the motions of which can be driven and accurately controlled by TENGs [35]. Sun was one of the first to design the triboelectric nanogenerator powered soft robot [36]. Liu et al. demonstrated a bioinspired triboelectric soft robot consisting of a soft-deformable body (referring to dielectric elastomer actuator) and two triboelectric adhesion feet. Driven by mechanical energy, it reached a maximum crawling speed of 14.9 mm/s on the acrylic surface. These two innovative and seminal works pioneered TENGs to power soft robot prototypes [37], broadening the applicability of TENGs by offering new insight into feasible and sustainable power source technologies for electrically responsive soft robots. But existing triboelectric soft robots are actuated with dielectric elastomer actuators. This kind of electro-active actuator material typically requires complex stacked configurations, a rigid frame, and prestretch to perform effectively. Besides, challenges in large driving voltage (over several thousand volts to reach full strain), large leakage currents, and power dissipation result in reaching electrical breakdown more easily [38, 39]. Notably, ferroelectric and electrostrictive polymers also require high input voltages; however, these kinds of polymers can be more compatibly coupled with TENG's high voltage because of its high impedance and voltage tolerant capability. A good example of this can be found in the work of Zhang et al. (2014) [32]. This study introduced an active piezoelectric micro-actuator based on planar sliding TENG for optical modulation, opening up new opportunities for TENG's applications in piezoelectric materials.

Trajectory manipulation, as well as actuation, is an essential function for soft robots, especially for those autonomous robots capable of responding intelligently to the unknown environment [20, 40]. Usually, hard-bodied robots can realize turning motions by adjusting gaits, which usually relies on complex rigid joints to achieve multi-redundancy motion control. Differently, soft robots, based on material deformation, have unmatched levels of flexibility and adaptability. But owing to low stiffness and modulus [20], their complex deformation is difficult to predict and control, reducing the capacity of loading and improving the difficulty of motion control. To summarize, one long-standing difficulty for soft robots is the absence of appropriate control mechanisms and trajectory manipulation.

As an emerging power source, the TENG has rapidly developed to a mainstream technique in the field of energy-harvesting and self-powered systems [28]. However, till now, the utilization of TENGs to actuate and control piezoelectric soft robots has not been thoroughly investigated. In this work, for the first time, we reported a triboelectric effect-driven piezoelectric soft robot (TEPSR) system, which is mainly composed of a well-designed rotary freestanding triboelectric nanogenerator (RF-TENG), an insect-scale tethered soft robot, and corresponding control module. Specifically, mechanical energy was converted into electricity to power the piezoelectric unimorph structure through a RF-TENG. Except for locomotion, to simultaneously execute the scheme of trajectory control, the energy produced by TENG was stored in a 4.4 nF capacitor through a full bridge rectifier. By accumulating opposite charges on the different plates, a full charge state of 450 direct current (DC) volts was obtained within 4 s. Then, the steering is achieved by applying high voltage to the left or right electrostatic footpad. The characteristics of moving and slope-climbing speed, payload capacity, as well as turning motion, have been measured under the power of RF-TENG. By maneuvering the robot around a maze, the actuation and manipulation capacity is intuitively verified. Furthermore, to confirm the feasibility of the actuation and control strategy on the autonomous prototype robot, two infrared sensors are added to execute an obstacle-avoiding mission in an unstructured environment. This work innovatively combines the nanogenerators with the piezoelectric soft robot, further expanding the applicability of TENGs as well as providing energy-harvesting schemes for piezoelectric soft robots.

2 Design and optimization

2.1 Structure and working principle

As sketched in Fig. 1(a), the triboelectric effect-driven piezoelectric soft robot system is mainly composed of three parts: RF-TENG, a piezoelectric-driven robot, and corresponding control module. In this system, as exhibited in Fig. 1(b), the piezoelectric soft robot is composed of a polyvinylidene difluoride/polyimide (PVDF/PI) unimorph actuator, supporting structures, and two electrostatic footpads. According to previous work [7, 8, 41], to drive a piezoelectric PVDF unimorph structure within minimal energy expenditure on reactive power, an alternating current (AC) driving power near the resonant frequency is an essential prerequisite. Compared with other energy schemes, TENG's AC output signal might be a decent option because of their low manufacturing and fabrication costs, outstanding resilience, remarkable stability, and environmental friendliness. However, considering that traditional transformers, crossover circuits, and multipliers face a sharp loss in transforming the power TENG produced [42], electrical parameters of the RF-TENG, such as frequency and voltage, should be directly compatible with the soft robot. The detailed design and working principle of RF-TENG and the soft robot proceed as follows.

2.1.1 Rotary freestanding triboelectric nanogenerator

There are four fundamental working modes of the triboelectric nanogenerators, including vertical contact-separation mode, lateral sliding mode, single-electrode mode, and freestanding triboelectric-layer mode [43], among which RF-TENG can realize high voltage and high-frequency output while improving the space utilization and maximizing the triboelectric charge generation and electrostatic induction, benefiting from the periodic-structure and mature printed circuit board (PCB) technology [44]. The three-dimensional (3D) structure diagram of the RF-TENG is shown in Fig. 1(c), which mainly includes two parts: a stator and a rotator. Copper (Cu) and polytetrafluoroethylene (PTFE), with a large difference in triboelectric negativity [45], were selected as the electrode and the freestanding triboelectric layer, respectively. To generate periodically changing electric field with compatible frequency, we designed the radial-arrayed RF-TENG, as shown in Fig. S1 in the Electronic Supplementary Material (ESM). It is noteworthy that adjacent electrodes in the stator, serving as positive and negative poles of the power supply, are divided by fine trenches.

Furthermore, non-neighboring electrodes are connected by inner or outer wires, forming two sets of separated electrodes. The detailed fabrication process of the RF-TENG is illustrated in the Method section. As illustrated in the cross-sectional view in Fig.

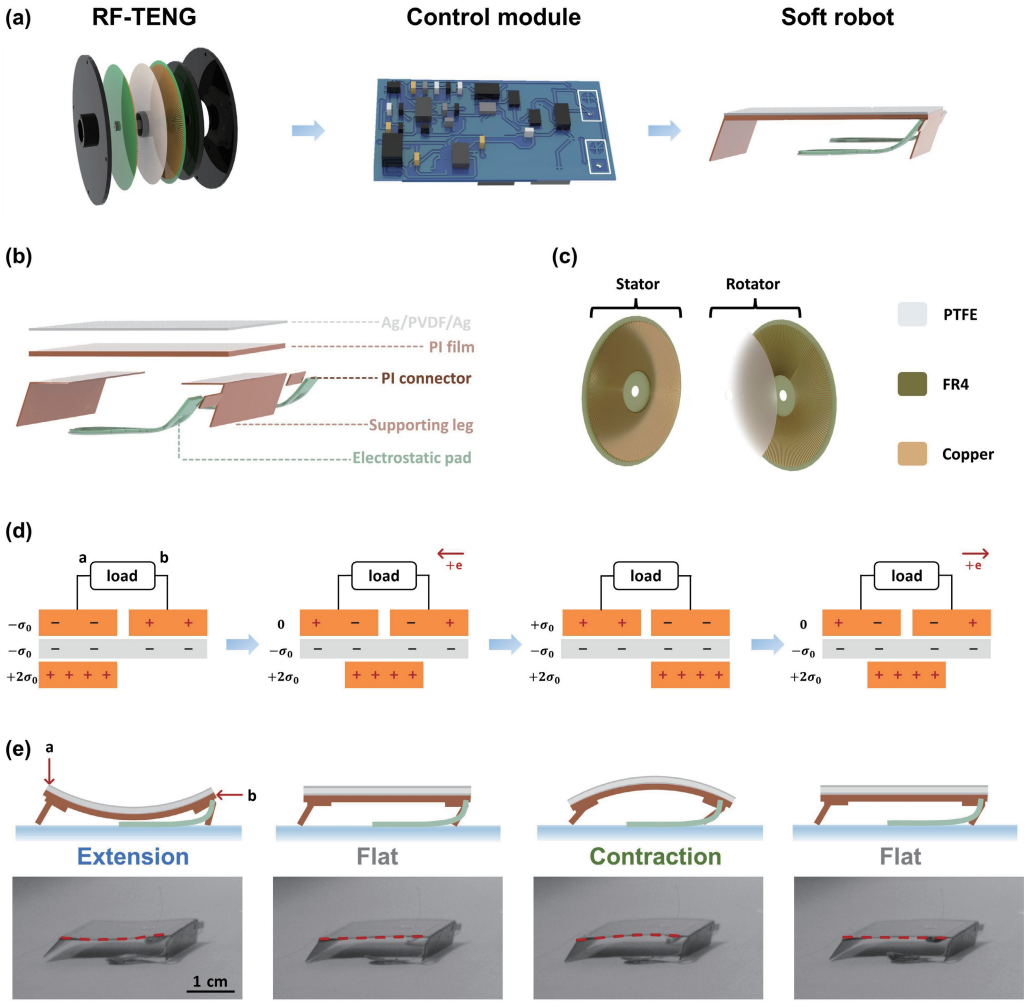

Figure 1 Schematic illustrations of the TEPSR system. (a) 3D structural schematic of the TEPSR system consists of the RF-TENG, a piezoelectric-driven robot, and corresponding control module. (b) Exploded view of the piezoelectric soft robot. (c) 3D structural schematic of the configuration of RF-TENG. (d) Illustration of producing triboelectric charges and electrostatic induction in one cycle. (e) Actuating mechanism of the piezoelectric unimorph robot with corresponding gait overview and a sequence of optical images captured the undulating gait of a prototype robot in one driving cycle.

1(d), the mechanism of power generation can be elaborated through a basic unit. Considering the rotator surface area differs from that of the PTFE, to maintain charge conservation, the charge density on the rotator surface is twice as much as that of PTFE surface. In the initial state, the left electrode, completely superimposed with a bottom metal grating, is negatively charged, and the adjacent electrode generates an equal amount of positive charge due to electrostatic induction. Between the two top electrodes, the electric potential difference is maximum value and the current is zero because of electrostatic balance. Then, after the rotator's relative slipping, the positive charge from the right electrode will shift to the left one and reach another static equilibrium. In the immediate state, charge flow reaches a balance at the half circle. As the bottom metal grid slides to the next electrode, the flow of charge reverses to screen the potential difference. The electric potential difference between the two electrodes results in continuous AC output (sharp peak signal) when the contact areas periodically change [46]. To verify the feasibility of the operation principle, we use the commercial finite element analysis software COMSOL Multiphysics to carry out the simulation of the electric potential distributions of the device, as shown in Fig. S2 in the ESM. Detailed simulated methods are provided in Section S1 in the ESM.

2.1.2 *Robot structure design*

In this work, a prototype soft robot (weight of 350 mg, size of 24 mm × 22 mm) was fabricated. The detailed structure can be divided into four functional parts: a soft-deformable body, the front legs, the tail, and two electrostatic footpads (Fig. 1(b)). The photograph of our soft robot is shown in Fig. S3 in the ESM. The detailed fabrication procedure of the soft robot is available in the Method section and also described in our previous work [8].

The detailed working principle of piezoelectric unimorph for continuous motions could be explained by Fig. S4 and Section S2 in the ESM, and also be divided into four driving processes as presented in Fig. 1(e). The top and bottom electrodes of the PVDF film are connected to the left and right electrodes of the RF-TENG (indicated in Figs. 1(d) and 1(e) by "a" and "b"), respectively. As the bottom metal grid slides over the two top electrodes, the electric potential difference varies accordingly. Under such AC voltages, the flat PVDF film can change its dimension in the d_{31} (piezo strain constant; when the charge is collected along the polarization axis, the force is applied at right angles to the polarization axis) direction because of the reverse piezoelectric effect. The PVDF/PI unimorph actuator has the advantage of providing curvature change rather than length change [47]. Therefore, the prototype soft robot can extend and contract periodically with legs striking the ground, generating an undulating gait that mimics the movement of a cockroach [7]. As a validation, the movements of the prototype robot were captured by a high-speed camera (V710, Phantom) in driving cycles (see Movie ESM1).

2.2 Parameter optimization and electromechanical properties characterization

According to Gauss theorem and previous research of RF-TENG [44, 48], when the edge effect and dielectric layers aspect ratio are negligible, the electric field line is assumed to be perpendicular to the surface of the films [42]. The V_{oc}–α relationship can be expressed as

$$V_{oc}(\alpha)=\begin{cases}\dfrac{2d\sigma_0}{\varepsilon_0\varepsilon_r} & \alpha=0\\ \dfrac{d\sigma_0}{\varepsilon_0\varepsilon_r}\left(\dfrac{\alpha_0-\alpha}{\alpha}-\dfrac{\alpha}{\alpha_0-\alpha}\right) & 0<\alpha<\alpha_0\\ -\dfrac{2d\sigma_0}{\varepsilon_0\varepsilon_r} & \alpha=\alpha_0\end{cases} \quad (1)$$

where V_{oc} is the open-circuit voltage between the two electrodes, d is the thickness of the PTFE layer, σ_0 is the triboelectric charge density of the PTFE surface, ε_0 is the permittivity of vacuum, ε_r is the relative dielectric constant of PTFE, α is the rotation angle of rotator from initial state, and α_0 is the central angle of a rotator electrode (with the same central angle of one single stator electrode).

The frequency of the alternating current (f) is

$$f=N\times\frac{\mathrm{RPM}}{60} \quad (2)$$

where N and RPM are the grid number and rotational speed (rpm) of the rotator, respectively. Previous research on the theoretical model confirms TENG can be considered as a voltage source coupled with a capacitor in series, the capacitance of which fluctuates through operation [49]. The internal capacitance of the RF-TENG $C_0(\alpha)$ is given by

$$C_0(\alpha)=N\frac{\varepsilon_0\varepsilon_r\pi(r_2^2-r_1^2)}{360d}\times\frac{(\alpha_0-\alpha)\alpha}{\alpha_0} \quad (3)$$

where r_2 and r_1 are the outer radius and inner radius of the rotator, respectively.

The PVDF composite film, treated as a parallel plate capacitor, can be calculated as

$$C_{load}=\frac{\varepsilon_d\varepsilon_0 lb}{t} \quad (4)$$

where ε_d, l, b, and t are the relative permittivity, length, width, and thickness of the PVDF, respectively. Substituting parameters [7] (ε_d = 12.83, ε_0 = 8.85 × 10^{-12} F/m, l = 24 mm, b = 22 mm, t = 28 μm) into Eq. (4), theoretical value of C_{load} is 2.14 nF, which has a good agreement with experimental value measured by LCR meter (LCR IM3536, HIOKI).

According to the equivalent circuit modeling of RF-TENG with outer load, the relationship between the open-circuit voltage $V_{oc}(\alpha)$ and the output voltage $V_{out}(\alpha)$ can be described by

$$V_{out}(\alpha)=V_{oc}(\alpha)\frac{C_0(\alpha)}{C_0(\alpha)+C_{load}} \quad (5)$$

Based on the model of elastic deformation of multilayers [50], the curvature R_{body} of the unimorph can repeatedly change under the applied voltage. The detailed derivation of the formulae is available in Figs. S5 and S6, and Section S3 in the ESM.

To be noticed, geometric parameters of the RF-TENG, including size, the unit central angle, and grids, as shown schematically in Fig. 2(a), have a significant impact on its output performance [48]. In this work, we first determined the values of outer radius r_2 = 120 mm and inner radius r_1 = 35 mm based on previous research of the RF-TENG [51]. Then simulation prediction was carried out to explore the effects of the central angle of a single rotator electrode α_0 and the grid number of the rotator N on the peak-to-peak output voltage with capacitive load C_{load}. Based on the analytical model established above, we employed MATLAB for the simulation of output voltage under various combinations of the unit central angle α_0 and grid number of the rotator N. With the constraints of geometric relations, $N\times\alpha_0$ should be less than 180°. The simulation results are given in Fig. 2(b), and three combinations (gray dots in Fig. 2(b)) of the above geometric parameters were selected to fabricate the RF-TENG. As a guidance, three combinations, 45, 90, and 180 gratings on the rotator corresponding to the center angles of 2°, 1°, and 0.5°, were conducted experiments to plot the output voltage versus number of grids and rotation rate in Fig. 2(c). Considering the resonance frequency of the robot is 300 Hz (AC square waves, supplied by amplifier and signal generator) [8], the rotation speed of the three rotors should be 400, 200, and 100 rpm, respectively. The first two designs can reach the voltage required by the robot, and the third design voltage decreases slightly, mainly because the edge effect of the electrode cannot be ignored as the number of grids increases. The following experiments are carried out on 45 grids.

3 Results and discussion

To verify the feasibility of the actuation scheme, a comparison experiment was conducted. As schematically depicted in Figs. 2(d) and 2(g), the former option is to connect the robot to the RF-TENG directly. In the latter case, the robot is connected to an amplifier (ATA-2082, Agitek) (magnification factor is 100), and the waveform generator (DG 1062Z, RIGOL) is used to generate the sinusoidal wave voltages (V_{p-p} = 5.6 V and f = 300 Hz). To quantify the power consumption in both cases, driving voltage (V) and corresponding current (I) are simultaneously measured by a data acquisition system, and the results are shown in Figs. 2(e) and 2(h). Besides, given a certain period of time T, the output energy in one cycle E and the average power consumption $\overline{P}_{in}$ can be calculated as the ringed area of the closed loop in the V–Q curve [52]

$$\begin{cases}E=\int_0^T VI\mathrm{d}t=\oint V\mathrm{d}Q\\ \overline{P}_{in}=\dfrac{1}{T}\int_0^T VI\mathrm{d}t=\dfrac{1}{T}\oint V\mathrm{d}Q\end{cases} \quad (6)$$

Sample measurements of instantaneous voltage and transferred charge are shown in Figs. 2(f) and 2(i). Conducted in MATLAB, the numerical integration results of output energy in one driving cycle are 314.59 and 350.36 μJ, corresponding to average power consumption of 94.38 and 105.11 mW, respectively. The electrical parameters in both cases share the same characteristics, and the RF-TENG exhibits excellent performance comparable to commercial signal sources and amplifiers, indicating the possibility of creating a self-powered system in the most straightforward way.

3.1 Rapid actuation of soft robot

Considering slight asymmetries in the robot body structure caused by fabrication and assembly imprecision led to the inability of the robot to run straightly for long periods of time, the robot was placed in an acrylic tube with a ruler on it for convenient measurement. Driven under AC voltages of various frequency (f), the experimental result is shown in Fig. 3(a). The moving speed peaks (10 cm/s) at the resonating frequency of 300 Hz (Movie ESM2), which results in less wasted energy, larger deformation, and greater forces at each cycle. We have to declare, in this case, the prototype robot moves at a lower speed than previously reported, mainly because the energy density of the spike pulse is

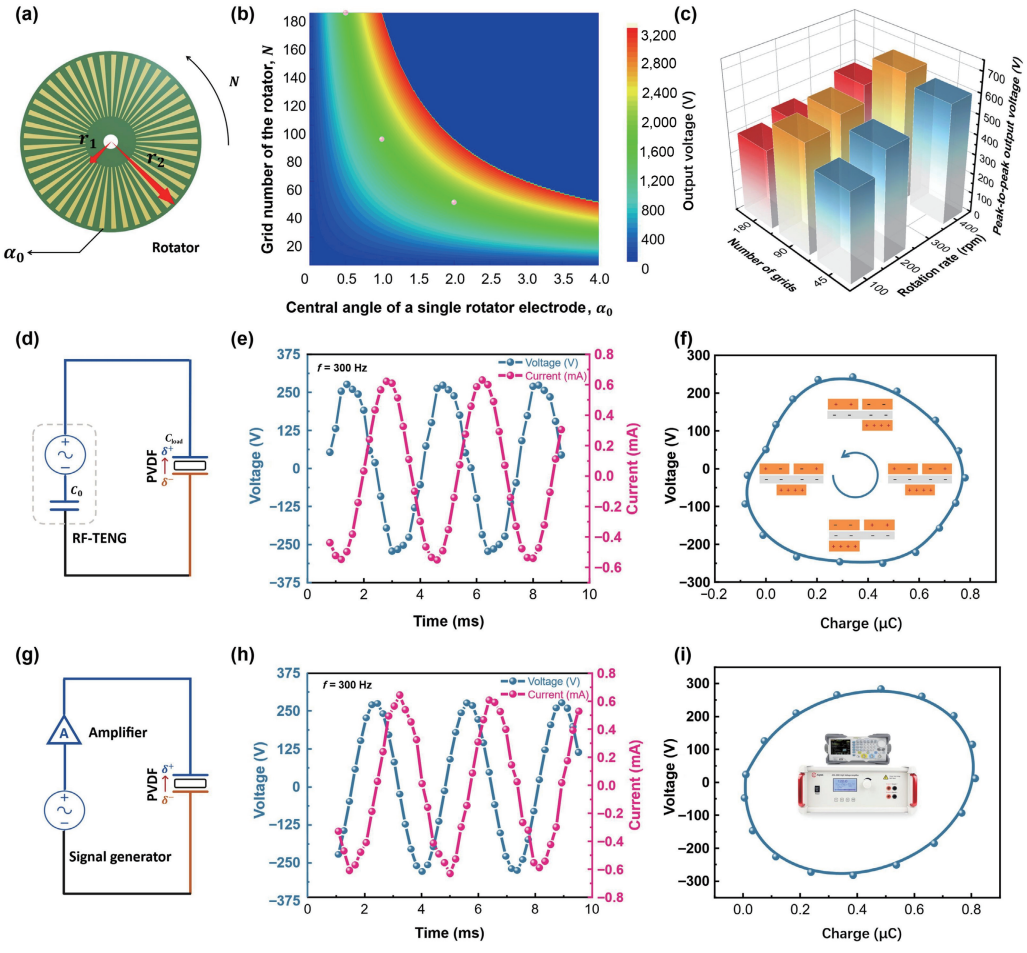

Figure 2 Geometric parameter optimization and electrical properties characterization. (a) View of the rotator and definition of geometric parameters. (b) Simulation results of the effects of the central angle of a single rotator electrode α_0 and the grid number N on the peak-to-peak output voltage with capacitive load C_{load}. (c) Peak-to-peak output voltage with capacitive load versus different grid numbers and rotation rates of the rotator. (d) Schematic diagram of the unimorph robot actuated by the RF-TENG. (e) Voltage and current measurement in 3 cycles of the prototype robot actuated by the RF-TENG at 300 Hz. (f) Cycle for energy output of TENG with the prototype robot. (g) Diagram of the unimorph robot driven by the signal amplification circuit. (h) Voltage and current measured in 3 cycles when operated by the signal amplification circuit at 300 Hz. (i) Cycle for energy output of the signal amplification circuit with the prototype robot.

lower than that of the square wave. From the graph of Fig. 3(a), analogous to behavior ascertained in natural insects [53], the running speed reduces at varying non-resonant frequencies of 100, 200, 400, and 500 Hz, respectively. Unless otherwise stated, all the experiments below were conducted at the resonating frequency to minimize energy dissipation.

In practical applications, climbing and carrying are common tasks for both animals and robots, we further study the slope climbing capability and load capacity of the prototype robot. The moving speed under different angles of inclination is demonstrated in Fig. 3(b) and Movie ESM3. The velocity of robot is reduced with slope angle increasing as expected, reaching 3.9, 3.1, and 1.1 cm/s corresponding to angles of 3°, 5°, and 7°. For payload capacity (extra supporting frames were added to support the heavy payload, and total weight of the additional components is about 61.2% of the original robot, illustrated by the inset shown in Fig. 3(c)), as the payload (Lego mounted in the center of mass (COM) of the robot, Lego Inc.) increases (Fig. 3(c)), as envisaged, the robot speed drops from 10 to 2 cm/s with a 2.8 g (8 times body weight) payload due to the reduction in the vibration amplitude. More details can be found in Fig. S7 and Section S4 in the ESM.

3.2 Energy efficiency and cost of transport (CoT)

Power consumption and transduction efficiency are important parameters in soft robot systems [20, 54]. Figure 3(d) depicts the power flow in the triboelectric soft robot system, where P_{in} is the input mechanical energy power (estimated 1.93 W), P_0 represents the power generated by the RF-TENG (estimated 778.2 mW), P_{TENG} is the power transmitted to the electronics (estimated 94.38 mW), P_{el} is the power applied on the piezoelectric actuator, and P_{PVDF} is the mechanical energy converted from the electrical energy. The ratio η between the electrical power P_0 and input mechanical power P_{in} is 40.33%, the power supply efficiency of the RF-TENG η_{TENG} is 12.13%, and the internal capacitance dissipates over 85% of the total electrical power. Besides, P_{TENG} is approximately equal to P_{el}, because the circuit board only acts a switch when conducting the scheme of actuation.

For the strength of one material's electromechanical response, indicated by its electromechanical conversion efficiency, can be calculated as the ratio of mechanical output energy to electrical input energy. In this work, the electromechanical conversion efficiency of PVDF actuator η_{PVDF} is 15.3%, higher than some typical DEA's efficiency (0.95% [20] and 5.6% [54]), of which the vast majority of the energy dissipates by DEAs' high-resistance electrodes.

In addition to the above two indicators, the CoT is a widely accepted and non-dimensional metric to compare the efficiency of dissimilar animals and robots, which can be defined as [55]

$$\mathrm{CoT} = \frac{P_{\mathrm{TENG}}}{mgv} = \frac{\frac{1}{T}\int_0^T VI\mathrm{d}t}{mgv} = 275 \tag{7}$$

where v is the system's (mass m) velocity under the power input

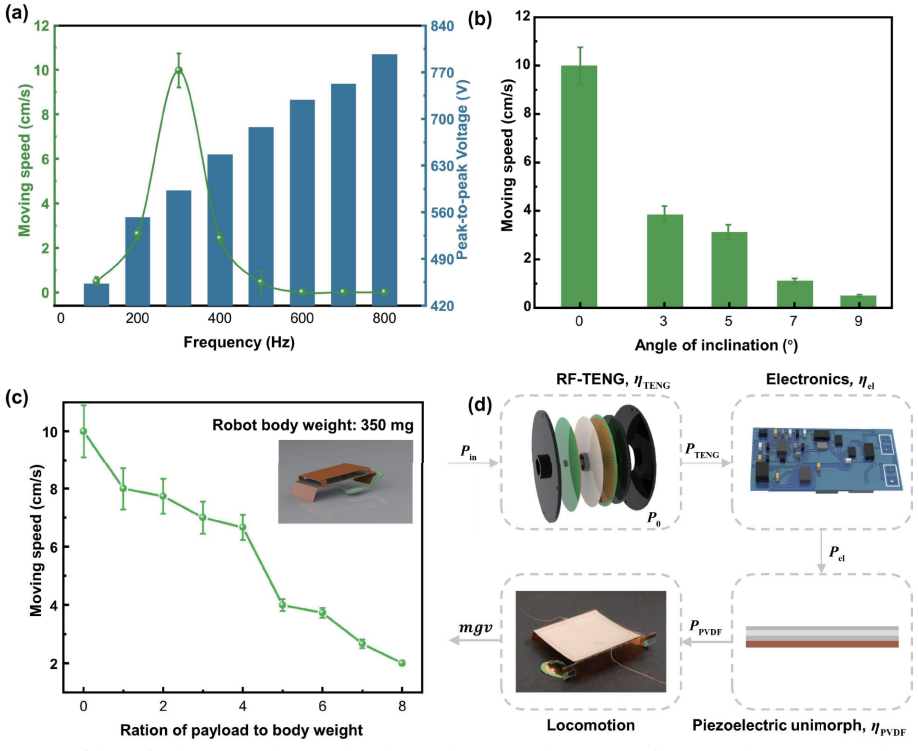

Figure 3 Motion characteristics of the soft robot. (a) Velocity and peak-to-peak output voltage versus frequency. (b) Moving speed versus angle inclination. (c) Moving speed with different payload masses. (d) Power flow in the triboelectric soft robot system, with moving speed at 10 cm/s.

to the system and g is the standard gravity. The CoT value of TEPSR is comparable to that of similar-sized HAMR-Jr [56] (also actuated by piezoelectric material), and typically lower than DEA soft robots [20]. More details are available in Figs. S8 and S9, and Section S5 in the ESM.

3.3 Agile trajectory manipulation of soft robot

Robots with legs usually need extra actuators and mechanisms to turn in, which would lead to energy consuming and weight gain. Notably, based on previous work [8, 57], controllable friction on the electroadhesive feet can provide a simple method and extra degrees of freedom for dynamic turning without additional actuators. In our previous work [8], we have designed an agile insect scale soft robot (3 cm by 1.5 cm, 65 mg) with trajectory maneuverability through adjusting the adhesion force. The basic principle is as follows, the slip that the robot's feet suffer when scuffing against the ground is influenced by friction. Slip is decreased by increasing friction on one of the robot's feet, which might lead to turning by making the robot pivot around that foot. Therefore, by modulating the friction force between the right and left electrostatic pads, the robot can produce movements with variable and controllable trajectories, such as straight, clockwise, and counterclockwise motions. The friction force is directly influenced by the electrostatic force generated by the applied electrical field (see Fig. S10 and Section S6 in the ESM). According to a standard model for eletroadhesion [58], the adhesion force is determined by the applied voltage V on the electrostatic footpad. The electrostatic force F_e is given by

$$F_e = \frac{1}{2} A \varepsilon_0 \varepsilon_r \frac{V^2}{d^2} = \frac{1}{2} A E^2 \tag{8}$$

where A is the area of the electrostatic footpad, ε_0 and ε_r are the permittivity of vacuum and dielectric constant of the material, respectively, d is the dielectric thickness, and E is the electrical field.

Then, the friction force on the pad can be obtained

$$f = \mu_0 (F_e + mg) \approx \mu_0 F_e = \frac{1}{2} \mu_0 \varepsilon_0 \varepsilon_r A \frac{V^2}{d^2} \tag{9}$$

where μ_0 is the friction coefficient between the substrate and pad, and mg is the gravity of the robot, which is negligible compared with the adhesion force. The steering can be controlled by adjusting the applied voltage on both pads. In order to generate a stable DC voltage applied on footpads, a full bridge rectifier was introduced, and Fig. 4(a) shows the schematic diagram.

For different capacitors, the rectified voltage by full bridge rectifier at different rotational rate (rpm) is shown in Fig. 4(b). In the graph, operating at the same rotational rate, it can be observed the rectified voltage increases to a steady value as the capacitance increasing. It can also be concluded that, when the capacitance is constant, voltage increment is observed as the rotational rate increasing. By connecting electrolytic capacitor as the storage device at the diode bridge output, operating at the rotational rate of 400 rpm, we obtained exponentially stored charge curves. As can be seen in Fig. 4(c), with capacitance increasing, the charged voltage and charging time increase. The bar chart in Fig. 4(d) illustrates the rectified voltage versus different capacitance at the rotational rate of 400 rpm. In Fig. 4(e), the adhesion force between the electrostatic pad on paper, polymer, and metal substrates is also measured under different capacitance. The friction force is shown to grow symmetrically regarding the capacitor. In addition, we also measure the centripetal acceleration when applying voltage only on the right foot-pad, which is shown in Fig. 4(f) (Movie ESM4). Considering the charging time and rectifier voltage, we finally choose a capacitor of 4.4 nF to obtain the DC voltage (power and energy consumption on the unimorph robot body are also given in Section S5 in the ESM after the rectifier is added).

In order to execute two schemes at the same time, that is, actuation and trajectory manipulation, the diagram is shown in Fig. 4(g). When the switch is hit to K_0, K_1, or K_2, the robot produces straight, left turn, or right turn, respectively. As depicted in Fig. 5(a) (Movie ESM5), the actuation and manipulation demonstration, as a validation of the feasibility of this strategy, are accomplished by maneuvering the robot around a maze with a 71 cm track in 28 s.

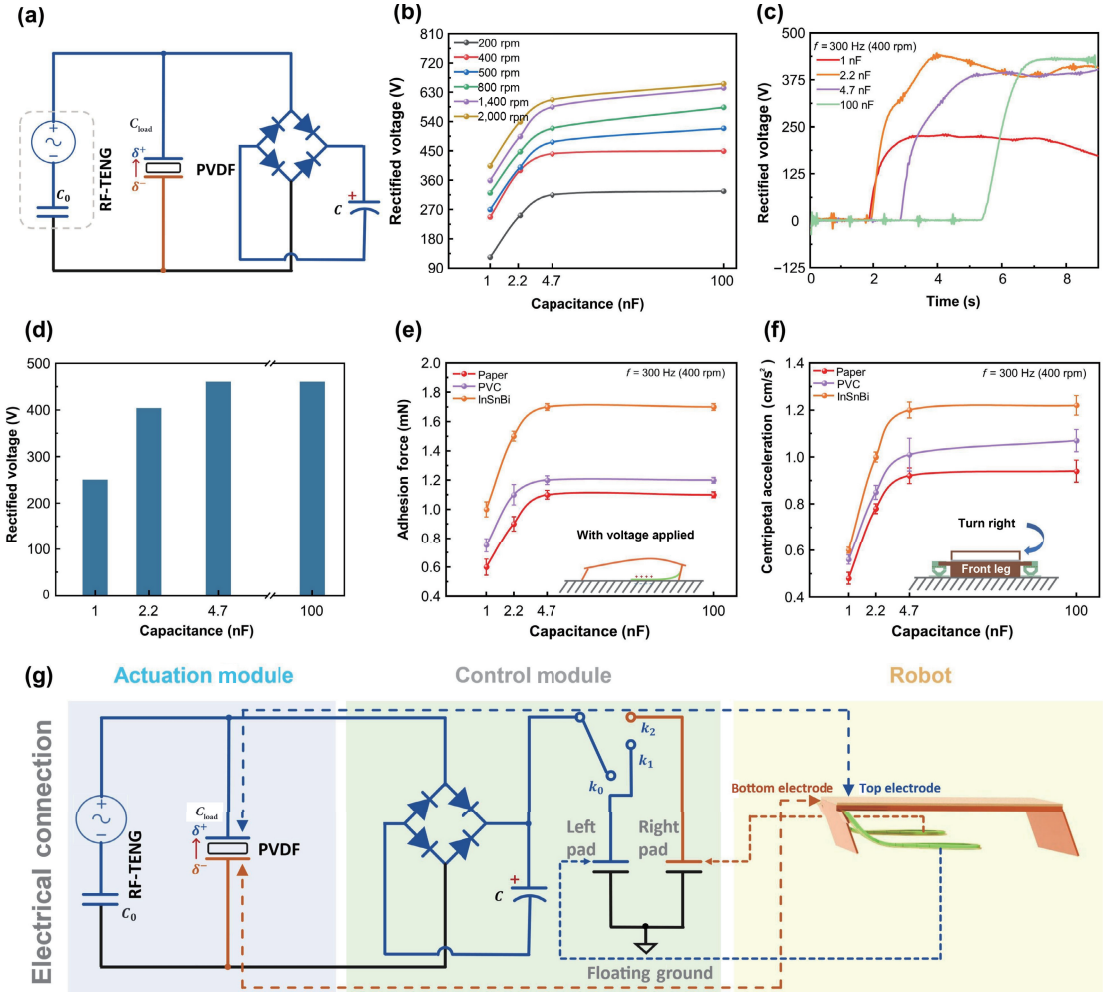

Figure 4 Steering principles and characteristics of the soft robot. (a) A schematic diagram of the electronic circuit for storage. (b) Rectified voltage versus capacitance at several different rotational speeds. (c) Charging curves for different capacitors. (d) Rectified voltage versus different capacitance at the rotational rate of 400 rpm. (e) Measured adhesion force between the electrostatic pad on paper, polymer, and metal substrates is also measured under different capacitance (inset shows rectified voltage is applied on the electrostatic footpad to generate adhesion force). (f) Centripetal acceleration versus capacitance on paper, polymer, and metal substrates (inset shows a diagram of the robot turning right). (g) Schematic illustration of the actuation and trajectory manipulation scheme with three key elements: the actuation module, control module, and robot. The top and bottom electrodes of the unimorph robot body are connected to RF-TENG directly. The left electrostatic front footpad (blue color) and the right electrostatic front footpad (orange color) are connected to different positions of the three-pole single-throw switch.

3.4 Autonomous feedback controls and video streaming

In recent years, great efforts have been devoted to equipping robotic systems with sensors to perceive the environment [21]. Here, to highlight the applicability and scalability of trajectory manipulation method in the autonomous robot, two reflective optical sensors with transistor output (TCRT1000 DIP4, the operating wavelength is 950 nm, Vishay Inc.) on board are used to realize obstacle avoidance in unstructured environments. The detailed working principle is presented in Fig. S11 and Section S7 in the ESM. The result shows that optical sensors enable the soft robot to perceive unpredictable environments, indicating its promising application for disaster rescue and interstellar exploration. Figure 5(b) shows that two reflective optical sensors can be easily installed onto an autonomous prototype robot, providing reactive obstacle avoidance in the wreckage.

Vision provides a means to perceive the world at a distance [59]. A tiny, lightweight, and power-efficient robotic vision system allows for flexibility and adaptation in front of the ever-changing environment. We use an onboard micro camera (RS-406C32-3.3V, 1/4-inch HD color CMOS) for image recording, constructing a real-time video transmission system by connecting to a computer, opening the possibility for control based on the vision data. Here we use 200 μm-thick PI film to construct the support structure. The performance of the camera is shown in Fig. 5(c), and the lower right corner inset shows images on the computer.

4 Conclusions

Considering lightweight, convenient, and sustainable high-voltage power supplies for soft robotics are still in high demand, in this work, we first developed triboelectric effect-driven piezoelectric soft robot, paving the way for piezoelectric soft robot driven by mechanical energy and pushing the boundaries of TENG's vast related applications. In such an electromechanical system, the scheme of actuation and manipulation can be satisfied simultaneously owing to the perfect combination. Besides, the corresponding control and feedback system with subsequent circuit design is constructed, providing a method for creating and controlling an autonomous, self-contained, and soft-bodied system. Meanwhile, a real-time visual monitoring platform is achieved successfully, which may have great applications in narrow space detection.

Towards improving moving speed and energy transduction efficiency, future studies could focus on how to increase the energy output density and reduce the internal resistance of RF-TENG. In practical application, wireless triboelectric nanogenerator compatible with the piezoelectric soft robot should be explored in the next research period.

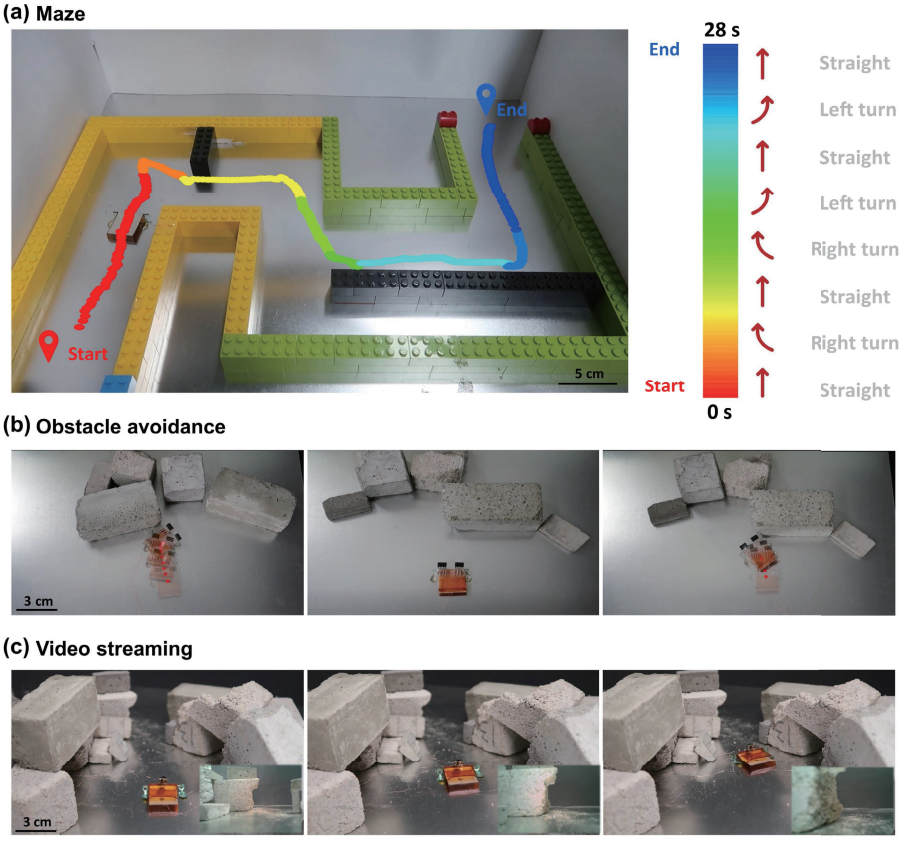

Figure 5 Demonstration of practical application. (a) A tethered prototype robot passed through a maze in barely 28 s. (b) By carrying two reflective optical sensors on top of the robot to avoid the existing obstacles. (c) "First-person" view onboard micro camera for video recording.

5 Method section

5.1 Characterization and measurement

Three prototype robots were fabricated and tested under the same experimental conditions. The experiment of each robot's locomotion characteristics was repeated ten times and averaged. A highspeed camera (V710, Phantom) was used to capture the movements of the prototype robot. The voltage applied on the soft robot was measured by DMM 7510 due to its relatively broad measurement range. A programmable electrometer (Keithley 6514) was employed to quantify the transferred charge and current flowing in the circuit. MATLAB and COMSOL Multiphysics software were adopted for the simulation of electrical parameters. The measurement of the friction forces between PI film and ground substrates is given in Section S8 in the ESM.

5.2 Fabrication of the RF-TENG

The disk-structured triboelectric nanogenerator was coaxially assembled by a free-standing rotator PCB (inside radius of 35 mm, the outside radius of 120 mm) installed on the shaft of a servo motor (110AEA18030-SH3, Times Brilliant Inc.) and a stator PCB (inside radius of 35 mm, the outside radius of 120 mm) fixed on a support plate, intimately contacting with each other. The 80-μm-thick PTFE tape (Chenguang Plastic Industry Co., Ltd.), consistent with the size of the rotator disc, was adhered to the rotator PCB surface firmly.

5.3 Fabrication of the soft robot

A 28-μm-thick PVDF film (PolyK Technologies, LLC), tailored to 24 × 22 mm, was deposited with 6-μm-thick silver (Ag) film as electrodes on both sides by slot die coating method. The sandwiched structure then was adhered to a PI tape (120 μm in thickness for polyimide and 25 μm in thickness for the adhesive, Keyun tape Inc.) by a vinyl cutter (CAMESO 3, Silhouette Inc.) to form PVDF/PI unimorph. The electrostatic footpad consisted of a 25-μm-thick polyethylene terephthalate (PET) frame and a 5-μm-thick PI film with 10 nm Cr/100 nm Al films as the electrode, which can be found in our previous work [8]. Eventually, these components were carefully folded and attached.

Acknowledgements

This work was supported by Shenzhen Fundamental Research Funds (No. JCYJ20220530143011026), and Science and Technology Plan projects in Sichuan Province (No. 2020YFSY0050).

Electronic Supplementary Material: Supplementary material (Movie ESM1: a high speed camera video for straight forward movements. Movie ESM2: rapid actuation of soft robot. Movie ESM3: climbing ability with slopes of different angles. Movie ESM4: steering control of the soft robot. Movie ESM5: out of the maze with trajectory manipulation. Section S1: finite element simulation of electric potential. Section S2: actuation mechanism of the soft robot. Section S3: theoretical analysis of the electrical properties of RF-TENG. Section S4: payload test of the soft robot. Section S5: energy efficiency and cost of transport calculation. Section S6: trajectory control strategy. Section S7: signal filtering and amplifying circuits. Section S8: measurement of the friction forces) is available in the online version of this article at https://doi.org/10.1007/s12274-022-5180-y.

References

[1] Rus, D.; Tolley, M. T. Design, fabrication and control of soft robots. *Nature* **2015**, *521*, 467–475.

[2] Deimel, R.; Brock, O. A novel type of compliant and underactuated robotic hand for dexterous grasping. *Int. J. Robot. Res.* **2015**, *35*, 161–185.
[3] Lai, Y. C.; Deng, J. N.; Liu, R. Y.; Hsiao, Y. C.; Zhang, S. L.; Peng, W. B.; Wu, H. M.; Wang, X. F.; Wang, Z. L. Actively perceiving and responsive soft robots enabled by self-powered, highly extensible, and highly sensitive triboelectric proximity- and pressure-sensing skins. *Adv. Mater.* **2018**, *30*, 1801114.
[4] Ren, Z. Y.; Hu, W. Q.; Dong, X. G.; Sitti, M. Multi-functional soft-bodied jellyfish-like swimming. *Nat. Commun.* **2019**, *10*, 2703.
[5] Kornbluh, R. D.; Pelrine, R.; Pei, Q. B.; Heydt, R.; Stanford, S.; Oh, S.; Eckerle, J. Electroelastomers: Applications of dielectric elastomer transducers for actuation, generation, and smart structures. In *Proceedings of SPIE 4698*, *Smart Structures and Materials 2002*: *Industrial and Commercial Applications of Smart Structures Technologies*, San Diego, USA, 2002, pp 254–270.
[6] Chen, S. H.; Tan, M. W. M.; Gong, X. F.; Lee, P. S. Low-voltage soft actuators for interactive human–machine interfaces. *Adv. Intellig. Syst.* **2022**, *4*, 2100075.
[7] Wu, Y. C.; Yim, J. K.; Liang, J. M.; Shao, Z. C.; Qi, M. J.; Zhong, J. W.; Luo, Z. H.; Yan, X. J.; Zhang, M.; Wang, X. H. et al. Insect-scale fast moving and ultrarobust soft robot. *Sci. Robot.* **2019**, *4*, eaax1594.
[8] Liang, J. M.; Wu, Y. C.; Yim, J. K.; Chen, H. M.; Miao, Z. C.; Liu, H. X.; Liu, Y.; Liu, Y. X.; Wang, D. K.; Qiu, W. Y. et al. Electrostatic footpads enable agile insect-scale soft robots with trajectory control. *Sci. Robot.* **2021**, *6*, eabe7906.
[9] Wang, W.; Lee, J. Y.; Rodrigue, H.; Song, S. H.; Chu, W. S.; Ahn, S. H. Locomotion of inchworm-inspired robot made of smart soft composite (SSC). *Bioinspir. Biomim.* **2014**, *9*, 046006.
[10] Felton, S. M.; Tolley, M. T.; Shin, B.; Onal, C. D.; Demaine, E. D.; Rus, D.; Wood, R. J. Self-folding with shape memory composites. *Soft Matter* **2013**, *9*, 7688–7694.
[11] Chen, T.; Bilal, O. R.; Shea, K.; Daraio, C. Harnessing bistability for directional propulsion of soft, untethered robots. *Proc. Natl. Acad. Sci. USA* **2018**, *115*, 5698–5702.
[12] Qian, X. J.; Chen, Q. M.; Yang, Y.; Xu, Y. S.; Li, Z.; Wang, Z. H.; Wu, Y. H.; Wei, Y.; Ji, Y. Untethered recyclable tubular actuators with versatile locomotion for soft continuum robots. *Adv. Mater.* **2018**, *30*, 1801103.
[13] Yang, Y.; Pei, Z. Q.; Li, Z.; Wei, Y.; Ji, Y. Making and remaking dynamic 3D structures by shining light on flat liquid crystalline vitrimer films without a mold. *J. Am. Chem. Soc.* **2016**, *138*, 2118–2121.
[14] Wang, E.; Desai, M. S.; Lee, S. W. Light-controlled graphene-elastin composite hydrogel actuators. *Nano Lett.* **2013**, *13*, 2826–2830.
[15] Breger, J. C.; Yoon, C.; Xiao, R.; Kwag, H. R.; Wang, M. O.; Fisher, J. P.; Nguyen, T. D.; Gracias, D. H. Self-folding thermo-magnetically responsive soft microgrippers. *ACS Appl. Mater. Interfaces* **2015**, *7*, 3398–3405.
[16] Tian, S. D.; Li, S. J.; Hu, Y. J.; Wang, W.; Yu, A. F.; Wan, L. Y.; Zhai, J. Y. A polymeric bilayer multi-legged soft millirobot with dual actuation and humidity sensing. *Sensors* **2021**, *21*, 1972.
[17] Peng, Y. D.; He, P. S.; Guo, R. Q.; Lin, L. W. Bioinspired light-driven soft robots by a facile two-mode laser engraving and cutting process. In *2021 21st International Conference on Solid-State Sensors*, *Actuators and Microsystems* (*Transducers*), Orlando, USA, 2021, pp 10–13.
[18] El-Atab, N.; Mishra, R. B.; Al-Modaf, F.; Joharji, L.; Alsharif, A. A.; Alamoudi, H.; Diaz, M.; Qaiser, N.; Hussain, M. M. Soft actuators for soft robotic applications: A review. *Adv. Intellig. Syst.* **2020**, *2*, 2000128.
[19] Hines, L.; Petersen, K.; Lum, G. Z.; Sitti, M. Soft actuators for small-scale robotics. *Adv. Mater.* **2017**, *29*, 1603483.
[20] Ji, X. B.; Liu, X. C.; Cacucciolo, V.; Imboden, M.; Civet, Y.; El Haitami, A.; Cantin, S.; Perriard, Y.; Shea, H. An autonomous untethered fast soft robotic insect driven by low-voltage dielectric elastomer actuators. *Sci. Robot.* **2019**, *4*, eaaz6451.
[21] Yang, G. Z.; Bellingham, J.; Dupont, P. E.; Fischer, P.; Floridi, L.; Full, R.; Jacobstein, N.; Kumar, V.; McNutt, M.; Merrifield, R. et al. The grand challenges of *Science Robotics*. *Sci. Robot.* **2018**, *3*, eaar7650.
[22] Xu, S.; Zhang, Y. H.; Cho, J.; Lee, J.; Huang, X.; Jia, L.; Fan, J. A.; Su, Y. W.; Su, J.; Zhang, H. G. et al. Stretchable batteries with self-similar serpentine interconnects and integrated wireless recharging systems. *Nat. Commun.* **2013**, *4*, 1543.
[23] Fan, F. R.; Tian, Z. Q.; Wang, Z. L. Flexible triboelectric generator. *Nano Energy* **2012**, *1*, 328–334.
[24] Bai, P.; Zhu, G.; Lin, Z. H.; Jing, Q. S.; Chen, J.; Zhang, G.; Ma, J. S.; Wang, Z. L. Integrated multilayered triboelectric nanogenerator for harvesting biomechanical energy from human motions. *ACS Nano* **2013**, *7*, 3713–3719.
[25] Chen, B.; Yang, Y.; Wang, Z. L. Scavenging wind energy by triboelectric nanogenerators. *Adv. Energy Mater.* **2018**, *8*, 1702649.
[26] Jiang, T.; Yao, Y. Y.; Xu, L.; Zhang, L. M.; Xiao, T. X.; Wang, Z. L. Spring-assisted triboelectric nanogenerator for efficiently harvesting water wave energy. *Nano Energy* **2017**, *31*, 560–567.
[27] Jia, M. M.; Guo, P. W.; Wang, W.; Yu, A. F.; Zhang, Y. F.; Wang, Z. L.; Zhai, J. Y. Tactile tribotronic reconfigurable p-n junctions for artificial synapses. *Sci. Bull.* **2022**, *67*, 803–812.
[28] Nie, J. H.; Chen, X. Y.; Wang, Z. L. Electrically responsive materials and devices directly driven by the high voltage of triboelectric nanogenerators. *Adv. Funct. Mater.* **2019**, *29*, 1806351.
[29] Wang, Z. L. On Maxwell's displacement current for energy and sensors: The origin of nanogenerators. *Mater. Today* **2017**, *20*, 74–82.
[30] Chen, X. Y.; Jiang, T.; Yao, Y. Y.; Xu, L.; Zhao, Z. F.; Wang, Z. L. Stimulating acrylic elastomers by a triboelectric nanogenerator-toward self-powered electronic skin and artificial muscle. *Adv. Funct. Mater.* **2016**, *26*, 4906–4913.
[31] Chen, X. Y.; Pu, X.; Jiang, T.; Yu, A. F.; Xu, L.; Wang, Z. L. Tunable optical modulator by coupling a triboelectric nanogenerator and a dielectric elastomer. *Adv. Funct. Mater.* **2017**, *27*, 1603788.
[32] Zhang, C.; Tang, W.; Pang, Y. K.; Han, C. B.; Wang, Z. L. Active micro-actuators for optical modulation based on a planar sliding triboelectric nanogenerator. *Adv. Mater.* **2015**, *27*, 719–726.
[33] Chen, X. Y.; Iwamoto, M.; Shi, Z. M.; Zhang, L. M.; Wang, Z. L. Self-powered trace memorization by conjunction of contact-electrification and ferroelectricity. *Adv. Funct. Mater.* **2015**, *25*, 739–747.
[34] Lee, J. H.; Hinchet, R.; Kim, T. Y.; Ryu, H.; Seung, W.; Yoon, H. J.; Kim, S. W. Control of skin potential by triboelectrification with ferroelectric polymers. *Adv. Mater.* **2015**, *27*, 5553–5558.
[35] Bu, T. Z.; Yang, H.; Liu, W. B.; Pang, Y. K.; Zhang, C.; Wang, Z. L. Triboelectric effect-driven liquid metal actuators. *Soft Robot.* **2019**, *6*, 664–670.
[36] Sun, W. J.; Li, B.; Zhang, F.; Fang, C. L.; Lu, Y. J.; Gao, X.; Cao, C. J.; Chen, G. M.; Zhang, C.; Wang, Z. L. TENG-bot: Triboelectric nanogenerator powered soft robot made of uni-directional dielectric elastomer. *Nano Energy* **2021**, *85*, 106012.
[37] Liu, Y.; Chen, B. D.; Li, W.; Zu, L. L.; Tang, W.; Wang, Z. L. Bioinspired triboelectric soft robot driven by mechanical energy. *Adv. Funct. Mater.* **2021**, *31*, 2104770.
[38] Jung, K.; Koo, J. C.; Nam, J. D.; Lee, Y. K.; Choi, H. R. Artificial annelid robot driven by soft actuators. *Bioinspir. Biomim.* **2007**, *2*, S42–S49.
[39] Shintake, J.; Rosset, S.; Schubert, B.; Floreano, D.; Shea, H. Versatile soft grippers with intrinsic electroadhesion based on multifunctional polymer actuators. *Adv. Mater.* **2016**, *28*, 231–238.
[40] Xu, P.; Wang, X. Y.; Wang, S. Y.; Chen, T. Y.; Liu, J. H.; Zheng, J. X.; Li, W. X.; Xu, M. Y.; Tao, J.; Xie, G. M. A triboelectric-based artificial whisker for reactive obstacle avoidance and local mapping. *Research (Wash. D. C.)* **2021**, *2021*, 9864967.
[41] Ma, K. Y.; Chirarattananon, P.; Fuller, S. B.; Wood, R. J. Controlled flight of a biologically inspired, insect-scale robot. *Science* **2013**, *340*, 603–607.
[42] Liu, S. Y.; Li, Y. Y.; Guo, W.; Huang, X.; Xu, L.; Lai, Y. C.; Zhang, C.; Wu, H. Triboelectric nanogenerators enabled sensing and actuation for robotics. *Nano Energy* **2019**, *65*, 104005.
[43] Wang, Z. L.; Chen, J.; Lin, L. Progress in triboelectric

nanogenerators as a new energy technology and self-powered sensors. *Energy Environ. Sci.* **2015**, *8*, 2250–2282.
[44] Han, C. B.; Zhang, C.; Tang, W.; Li, X. H.; Wang, Z. L. High power triboelectric nanogenerator based on printed circuit board (PCB) technology. *Nano Res.* **2015**, *8*, 722–730.
[45] Zou, H. Y.; Zhang, Y.; Guo, L. T.; Wang, P. H.; He, X.; Dai, G. Z.; Zheng, H. W.; Chen, C. Y.; Wang, A. C.; Xu, C. et al. Quantifying the triboelectric series. *Nat. Commun.* **2019**, *10*, 1427.
[46] Fan, F. R.; Lin, L.; Zhu, G.; Wu, W. Z.; Zhang, R.; Wang, Z. L. Transparent triboelectric nanogenerators and self-powered pressure sensors based on micropatterned plastic films. *Nano Lett.* **2012**, *12*, 3109–3114.
[47] Du, Y. H.; Peng, B.; Zhou, W.; Wu, Y. C. A piezoelectric water skating microrobot steers through ripple interference. In *2022 IEEE 35th International Conference on Micro Electro Mechanical Systems Conference* (*MEMS*), Tokyo, Japan, 2022, pp 644–647.
[48] Zhu, G.; Chen, J.; Zhang, T. J.; Jing, Q. S.; Wang, Z. L. Radial-arrayed rotary electrification for high performance triboelectric generator. *Nat. Commun.* **2014**, *5*, 3426.
[49] Niu, S. M.; Wang, Z. L. Theoretical systems of triboelectric nanogenerators. *Nano Energy* **2015**, *14*, 161–192.
[50] Hsueh, C. H. Modeling of elastic deformation of multilayers due to residual stresses and external bending. *J. Appl. Phys.* **2002**, *91*, 9652–9656.
[51] Ghaderiaram, A.; Bazrafshan, A.; Firouzi, K.; Kolahdouz, M. A multi-mode R-TENG for self-powered anemometer under IoT network. *Nano Energy* **2021**, *87*, 106170.
[52] Zi, Y. L.; Niu, S. M.; Wang, J.; Wen, Z.; Tang, W.; Wang, Z. L. Standards and figure-of-merits for quantifying the performance of triboelectric nanogenerators. *Nat. Commun.* **2015**, *6*, 8376.
[53] Dudley, R. *The Biomechanics of Insect Flight*: *Form*, *Function*, *Evolution*; Princeton University Press: Princeton, 2002.
[54] Chen, Y. F.; Zhao, H. C.; Mao, J.; Chirarattananon, P.; Helbling, E. F.; Hyun, N. S. P.; Clarke, D. R.; Wood, R. J. Controlled flight of a microrobot powered by soft artificial muscles. *Nature* **2019**, *575*, 324–329.
[55] Kim, S.; Wensing, P. M. Design of dynamic legged robots. *Foundat. Trends® Robot.* **2017**, *5*, 117–190.
[56] Jayaram, K.; Shum, J.; Castellanos, S.; Helbling, E. F.; Wood, R. J. Scaling down an insect-size microrobot, HAMR-VI into HAMR-Jr. In *2020 IEEE International Conference on Robotics and Automation* (*ICRA*), Paris, France, 2020, pp 10305–10311.
[57] Chen, A. S.; Bergbreiter, S. Electroadhesive feet for turning control in legged robots. In *2016 IEEE International Conference on Robotics and Automation* (*ICRA*), Stockholm, Sweden, 2016, pp 3806–3812.
[58] Koh, K. H.; Chetty, R. M. K.; Ponnambalam, S. Modeling and simulation of electrostatic adhesion for wall climbing robot. In *2011 IEEE International Conference on Robotics and Biomimetics*, Karon Beach, Thailand, 2011, pp 2031–2036.
[59] Iyer, V.; Najafi, A.; James, J.; Fuller, S.; Gollakota, S. Wireless steerable vision for live insects and insect-scale robots. *Sci. Robot.* **2020**, *5*, eabb0839.